BEILSTEIN ARCHIVES

This open access document is posted as a preprint in the Beilstein Archives at https://doi.org/10.3762/bxiv.2022.14.v1 and is considered to be an early communication for feedback before peer review. Before citing this document, please check if a final, peer-reviewed version has been published.

This document is not formatted, has not undergone copyediting or typesetting, and may contain errors, unsubstantiated scientific claims or preliminary data.

Preprint Title Influence of water contamination on the sputtering of silicon with low energy argon ions investigated by Molecular Dynamics simulations.

Authors Grégoire R. N. Defoort-Levkov, Alan S. Bahm and Patrick Philipp

Publication Date 17 März 2022

Article Type Full Research Paper

Supporting Information File 1 Ar_Si_Angles_Publication_Final_Version_Supporting_Information_09032022.docx; 1.1 MB

ORCID® iDs Grégoire R. N. Defoort-Levkov - https://orcid.org/0000-0001-8514-3817

License and Terms: This document is copyright 2022 the Author(s); licensee Beilstein-Institut.

This is an open access work under the terms of the Creative Commons Attribution License (https://creativecommons.org/licenses/by/4.0). Please note that the reuse, redistribution and reproduction in particular requires that the author(s) and source are credited and that individual graphics may be subject to special legal provisions. The license is subject to the Beilstein Archives terms and conditions: https://www.beilstein-archives.org/xiv/terms.
The definitive version of this work can be found at https://doi.org/10.3762/bxiv.2022.14.v1

Influence of water contamination on the sputtering of silicon with low energy argon ions investigated by Molecular Dynamics simulations.

Grégoire R.N. Defoort-Levkov*[1,2], Alan Bahm [3], Patrick Philipp *[1]

1 – Advanced Instrumentation for Nano-Analytics (AINA), Materials Research and Technology Department (MRT), Luxembourg Institute of Science and Technology (LIST), 4422 Belvaux, Luxembourg.

2 – University of Luxembourg, 4365 Esch-sur-Alzette, Luxembourg.

3 – Thermo Fisher Scientific, Hillsboro, OR, 97124, USA

Email: Patrick Philipp – Patrick.philipp@list.lu

* Corresponding author

The manuscript was written through contributions of all authors. All authors have given approval to the final version of the manuscript.

Abstract

Focused ion beams (FIB) are a common tool in nanotechnology for surface analysis, sample preparation for electron microscopy and atom probe tomography, surface patterning, nanolithography, nanomachining and nanoprinting. For many of these applications, a precise control of the ion-beam induced processes is essential. The effect of contaminations on these processes has not been explored thoroughly but can often be substantial, especially for ultralow impact energies in the sub-keV range. In this paper we investigate by molecular dynamics (MD) simulations how one of the most

commonly found residual contaminations in vacuum chambers, i.e. water, adsorbed on a silicon surface, influences sputtering by 100 eV argon ions. The incidence angle was changed from normal incidence close to grazing incidence. For the simulation conditions used in this work, the adsorption of water favours the formation of defects in silicon by mixing of the hydrogen and oxygen atoms into the substrate. The sputtering yield of silicon is not changed significantly by the contamination, but the fraction of hydrogen and oxygen atoms that is sputtered depends largely on the incidence angle. This fraction is largest for incidence angles between 70 and 80 degrees defined with respect to the sample surface. Overall, it changes from 25% to 65%.

Keywords

Molecular dynamics, Simulations, Silicon, Contamination, Water, Argon ions, ion bombardment, Angle dependency, Low energy.

Introduction

Focused ion beams (FIB) play an increasingly important role in materials research areas such as nano-analysis (e.g. secondary ion mass spectrometry (SIMS)[1–3] and sample preparation for transmission electron microscopy (TEM)[4], atom probe tomography (APT)[5] and ion beam analysis used for life sciences applications[6],[7]), surface patterning,[8] nanolithography,[9] nanomachining,[10,11] and nano-printing at room-[12] and cryo-temperature[13]. The development of nanotechnology relies on lower ion beam energies and smaller spot sizes to reduce the thickness of the layer damaged by ion beams, and to increase the lateral resolution for precise machining and sample characterization. For most of these applications, the quality of the sample

surface and its cleanliness are essential and therefore highly controlled. Depending on the application, the ion beam energy is in the range of 10 to 30 keV when small spot sizes are required (i.e. spot sizes in the nm range) and at a few keV or even in the sub-keV range when low surface damage or minimized atomic mixing is required. One example is low-energy depth profiling SIMS to resolve thin films in multi-layered samples.[14]

Another example is TEM sample preparation, where the achievement of highest lateral resolutions in the subsequent TEM analysis requires thicknesses of lamellae between 10 and 20 nm, but goes along with a typical amorphous layer of 2 to 4 nm formed during the sample preparation by FIB milling.[15–17] Such an amorphous layer represents a substantial part of the thickness of the sample and the information coming from this part does not correspond to the initial sample structure. Minimizing the thickness of this amorphous layer during FIB milling is essential because most samples analysed in high precision instruments will be prepared using this method. This can be best achieved using low beam energies, ideally in the sub-keV range,[18] since low energy ion beams (under 500 eV) produce a thinner amorphous layer due to their lower penetration depth. Investigations performed with low energy argon ions[15],[19],[20] have shown that the current model describing the sputter yields and the sputtering processes (such as sputtering threshold and the amorphization process) does not fit with experimental data, leading to discrepancies that cannot be ignored.

Contaminants on the sample surface can also play a critical role during the milling process: water can be found on nearly every sample surface.[21] For example, in a vacuum chamber at a pressure of 10^{-8} mbar, there are still 10^{6} to 10^{9} molecules per cm^{3}. This contaminant has a strong impact on the ion beam process by modifying the

sputtering processes. Even under an ultrahigh vacuum of 10^{-12} mbar there are still 10^4 molecules.cm^{-3} remaining in the experimental chamber, thus making water by far the most found contaminant. These assumptions can be confirmed by SIMS experiments.[22] It is therefore safe to assume that most experimental chambers able to hold a vacuum between 10^{-6} to 10^{-10} mbar will contain water molecules that will interact with the sample surface. Water has been widely studied [23–26] and is well described by many simulation tools available to model the samples in such extreme cases.

Nowadays, very little is known about the influence of contaminations on the amorphization process under ion irradiation. Thanks to Molecular Dynamics (MD) simulations, a wide range of materials properties and process parameters can be reproduced.[27–29] In this paper, we are using MD simulations to study the sputtering of a surface with a water contamination by sub 500 eV ions, the information of interest being the chemical reactions occurring at and below the sample surface, as well as the mixing of the contaminant layer into the sample. The ReaxFF reactive force field will be used for this work.[30] ReaxFF force fields are specifically tuned for a set of atomic interactions. They are developed from quantum calculations and are adapted for MD simulations, providing faster calculations than pure QED/DFT and more information than classical MD/BCA simulations. ReaxFF simulations can cover a broad range of applications: from DNA molecule bombardments with heavy atoms[31] to graphene layers deposition on copper surfaces.[32] Numerous simulations using the ReaxFF potential have been conducted in the past years, several describing the sample with contaminants interactions (such as water or organic particles).[33–35]

To understand how the water layer influences the amorphization process, we designed metrics aiming to characterize the degree of amorphization in the sample. Previous works have tried to give a broader picture of the phenomenon in solids or in crystals[36], by using a very small sample size and performing an exhaustive study on the bond orders and the bond length average (gaussian core model), as well as analysing the granularity of the system in liquid/solid phases, but these methods were designed using a limited sample size of up to a few hundreds of atoms. Other studies have tried to elaborate a local-metric for condensed phase environments,[37] giving a good descriptor for phase transitions. While they provide good results for a specific crystalline structure, they are tedious to adapt to other structures. In this paper, we developed a simple metric based on bond length variations, which can be easily adapted to different crystalline structures to characterize sample amorphization, and also study sputtering surfaces exposed to residual water molecules.

Computational methods

Force fields

The ReaxFF force field differs from other established force fields, as it aims to bridge between quantum mechanics (QM) and classical MD. QM algorithms are limited to small sized samples (up to a few hundreds of atoms) due to the difficulty to solve Schrödinger equations for many-body systems, and classical MD make the assumption of fixed bonds, and usually do not include complex chemical reactions. ReaxFF captures the dynamic nature of bond formation and breaking, based on bond-order calculation from interatomic distances. ReaxFF also includes non-bonded

terms like Van der Waals and Coulombic interactions in the energy calculation, resulting in a sum of partial energies[38]. For all simulations described in this paper, the ReaxFF force field developed by *van Duin et. al.*[34] for the Si-C-O-H, system, $ReaxFF_{SiOCH(2019)}$ is used. To reproduce the interaction between argon ions and silicon, hydrogen, and oxygen atoms, we used DFT simulations to simulate the potential energy between each of these pairs (e.g., Ar-Ar, Ar-Si, Ar-H and Ar-O). Once extracted, the potential energy was fitted using a Morse potential. The Morse potential is described in the equation (1):

$$E_{syst} = D_0\left[e^{-2\alpha(r-r_0)} - 2e^{-\alpha(r-r_0)}\right] \quad (1)$$

where r represents the interatomic distance in distance units, r_0 the interatomic distance in equilibrium state (also in distance units), D_0 the depth well in energy units (defined per atomic interaction and related to the molecule dissociation energy), and α the control parameter on the well thickness, proportional to the curvature of the potential at its origin, in inverted length units.[39] The fit of the Morse potential can be seen in the **figure 1** for the Ar – Si bond, the rest of the fit can be found in the supporting information.

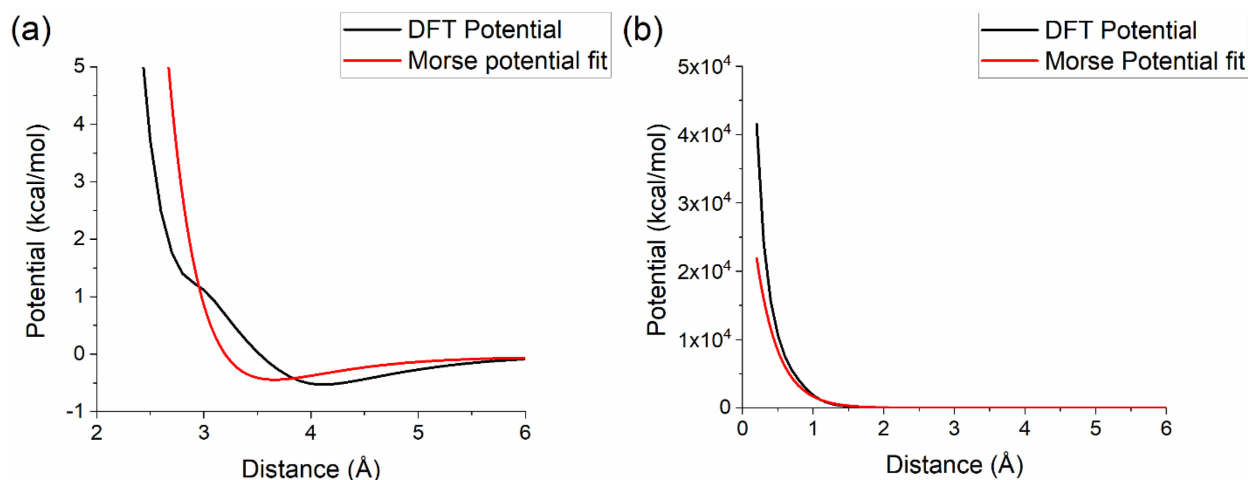

Figure 1: Fit of the DFT data for the Argon - Silicon potential in the 2 - 6 Å region, with (a) the potential well, and (b) the entire potential.

The ReaxFF potential is used to model the damage cascade and the collisions between silicon, hydrogen, and oxygen particles. An hybrid pair style[40] was used in the MD simulations to match both the ReaxFF potential (for Si – Si, Si – O, Si – H, O – O, O – H and H – H bonds) and the Morse potential (for Ar – Si, Ar – O, Ar – H and Ar – Ar interactions). The charge equilibration for the ReaxFF potential was performed using the algorithms developed by *Rappé et. al*,[41–43] namely QEq, allowing charge distributions to be calculated according to geometry. Due to the dynamic nature of bonds and geometrical configurations, the charge distribution QEq is performed every 10 time steps during the simulation of ion bombardment. During the deposition of the water on top of the silicon sample, the charge equilibration was performed at each step to fully describe the deposition of the contaminant on top of the sample.

Molecular Dynamics simulations

MD simulations on argon bombardment of a silicon surface were carried using the LAMMPS code.[44] A pristine silicon sample containing 5248 atoms was created and used as reference sample. On top of this sample was added a water layer to study the

effect of contaminations. Periodic boundary conditions are applied in x and y directions, with some vacuum above and below the sample in z direction.

In detail, after an initial energy minimization, the pristine sample was equilibrated using the Stillinger-Weber potential to obtain the dimers formed on the Si (100) surface,[21,45] with a timestep of 0.1 fs for 1 ns. The Langevin thermostat[46] was set to 300K in a micro-canonical ensemble (NVE) aiming to reproduce a canonical ensemble (NVT) at room temperature, avoiding the constraints of the canonical ensemble integration in LAMMPS.

The equilibration was continued with the ReaxFF potential for another 500 ps. The largest displacements observed in the sample being vibrational motions due to a temperature of 300 K (between 0.5 to 1 fs), the timestep was chosen to limit the maximum displacement between steps to one tenth of that motion, resulting in a 0.1 fs timestep for the simulations. Furthermore, as ReaxFF tends to reach a better stability at a shorter timestep, a variable timestep was defined between 0.05 and 0.1 fs, with a maximal allowed energy variation per atom between each step of 5 eV. This process allowed to limit the maximum displacement of atoms per timestep while the damage cascade happened and to increase it after the energy dissipated into the system. During the ion irradiation simulations, only the bottom slab of the sample (1 lattice high) was set in a NVT ensemble using the same methodology, in order to reproduce a heat-bath effect[47]. The remaining atoms were kept in the NVE ensemble in order to avoid any impact of the thermostat on the collision cascade.

Once properly equilibrated, the simulation of argon bombardment of pristine Si(100) was run for 50 ps, which was enough for the modelling of energy dissipation and sputtering, then thermalized to 300K. The last script was set to end as soon as the computed mean temperature reached 300K. The whole process was repeated until 500 ion impacts had been simulated. Compared to experiments, the time between two

ion impacts needed to be reduced by several orders of magnitude due to computational constraints, i.e., a few hundred picoseconds in simulations compared to µs in experiments, leading to an overall higher irradiation density yet keeping the sample at room temperature. To reproduce an ion beam, the initial positions of the argon ions were randomized in the surface plane. Each simulation set consisted of 500 irradiation events at a set incidence angle and an impact energy of 100 eV. For a surface area of 18.9 nm², this corresponds to a fluence of 2.6×10^{15} atoms.cm^{-2}. The simulations were carried out for incidence angles of 0, 20, 30, 45, 65, 72, 75, 83 and 85 degrees with respect to the surface normal. These angles were selected to cover a good sample of the 0 – 85° range, including angles of specific interest , i.e. 72° and 83° represent a channelling angle for Si(100)[48] and a grazing incidence angle frequently used in TEM lamellae preparation[49] for Si(100). A visualization of a set of simulations can be seen in the **figure 2**, and the global parameters of the simulations can be seen in the **Table 1**.

To prepare the contaminated sample, a layer of water was simulated in an isenthalpic-isobaric ensemble (NPT) for 500 ps, with a dedicated ReaxFF potential for hydrogen and oxygen, $ReaxFF_{OH(2017)}$.[24] Once the energy was properly minimized, the water layer was deposited on top of the pristine silicon sample in the NVE ensemble for up to a µs in order to reproduce the gradual contamination of the sample by residual gas molecules. After water deposition, a series of irradiation simulations was carried out using the same conditions than for the pristine sample.

	Surface (nm²)	**N° of Impacts**	**Energy (eV)**	**Fluence (ions/cm²)**
Simulations	18.9	500	100	2.6×10^{15}

Experiments	-	-	-	10^{16} - 10^{17}

Table 1: References of the simulation parameters, and parallel to instrument experiments conducted on SIMS / FIB instruments with the fluence.

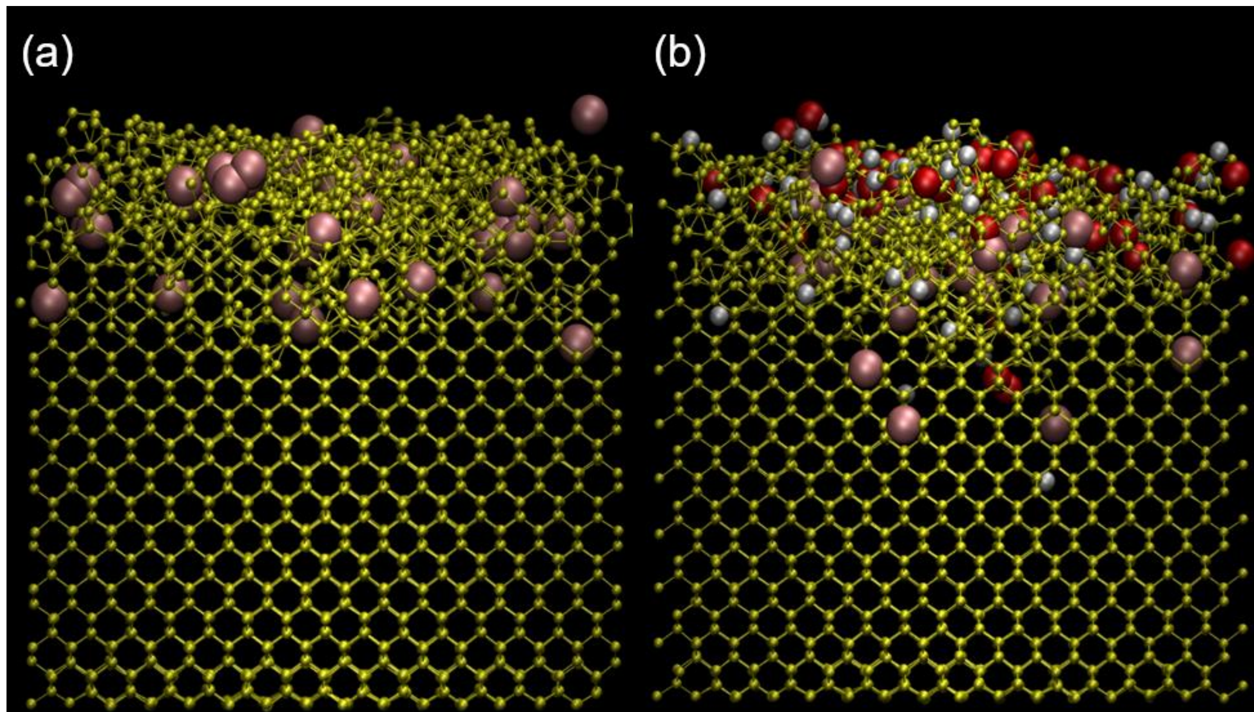

Figure 2: Representations of the (a) clean and (b) contaminated samples, with silicon atoms in yellow, oxygen atoms in red, hydrogen atoms in white, and argon atoms in pink. Both samples were bombarded at 45° and 100 eV and are viewed from the (110) direction after 500 irradiation events.

Results and Discussion

Sample characteristics and contaminant effects

At first, the bond length distributions were calculated to observe the effect of the water contaminant on these distributions. The nominal Si – Si bond in a diamond lattice is 2.358 Å. **Figure 3** shows the distributions for both samples before ion bombardment. For the Si-Si bonds, the most probable bond length is at the correct length, but a

significant number of bonds are in the 2.1 Å region. This can be explained by dimers appearing on the top and bottom surfaces and which have a nominal bond length (for Si dimers) of 2.1 Å.

The distribution for the contaminated sample shows two additional regions: the region between 0 and 2 Å and the region between 2.6 and 3.3 Å. The smallest bond length around 1 Å is due to the O – H bonds[50] in the water molecules. The second peak observed at around 1.4 to 1.7 Å is associated to both Si – H (1.56 Å)[51] and Si – O (1.58 Å)[52] bonds. The Si – H bonds are located near the surface between dimer Si atoms and some of the H atoms of the water after the reaction between silicon and oxygen leading to the splitting of the water molecules. Studies have suggested that oxygen dissociates on a single Si – Si dimer, allowing for the recombination of the dissociated hydrogens with Si surface atoms.[53] Some counts are also measured between 2.6 and 3.2 Å, which come from the amorphization of regular Si – Si bonds due to Argon collisions. Since most of the Si – O and Si – H bonds are shorter than these counts, it is safe to assume that the local disorder induced by reactions between water molecules and the sample surface tends to disorganize the silicon lattices. These bonds are longer than the ones of the crystalline structure, and their distribution follows a gaussian distribution. Both distributions are shown in **figure 4**, showing the evolution of the counts with respect to the number of bombardments, i.e. with increasing fluence.

Furthermore, **figure 4** shows how the 500 impacts have modified the bond length distributions: the counts related to amorphous bond (between 2.6 and 3.2 Å) have augmented clearly, with a reduction in the O – H bond counts (for the contaminated sample). Hence, most of the water adsorbed on the sample surface is either fractioned and mixed in the sample with repeated argon impacts, creating more Si – H and Si – O bonds, or sputtered from the sample surface.

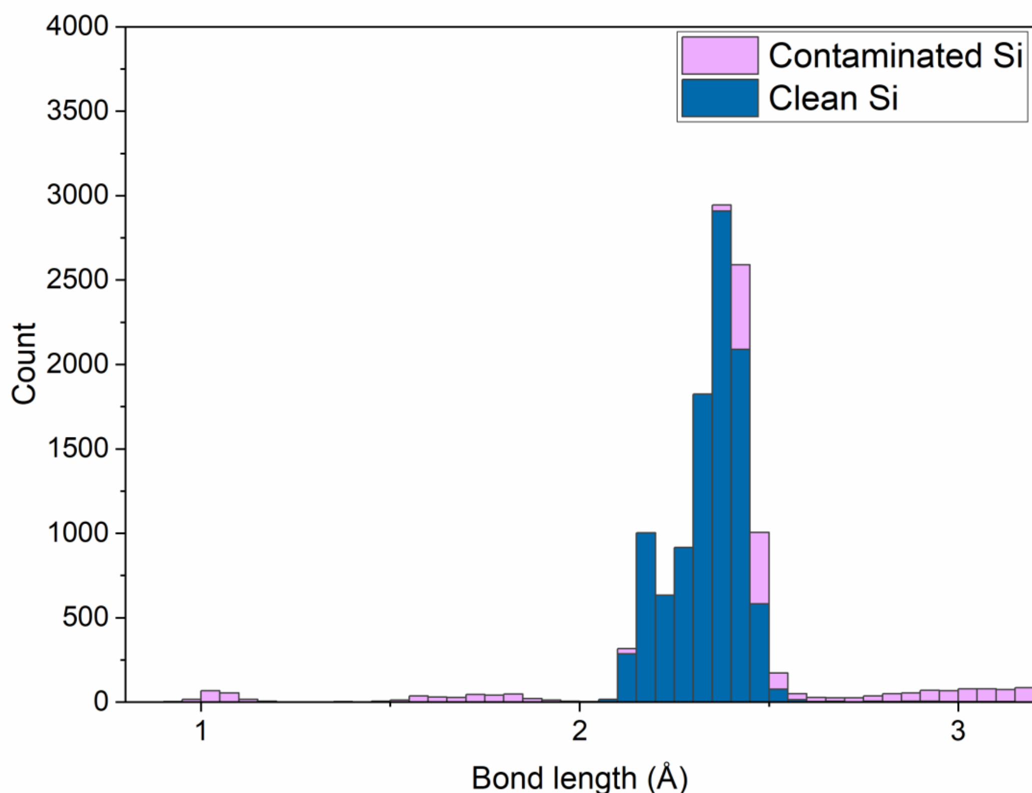

Figure 3: Bond length distributions for the pristine sample (a) and the contaminated sample (b) indifferently from the particle type with a cut-off at 3.2 Å (at which distance the distribution for the 2nd neighbours starts).

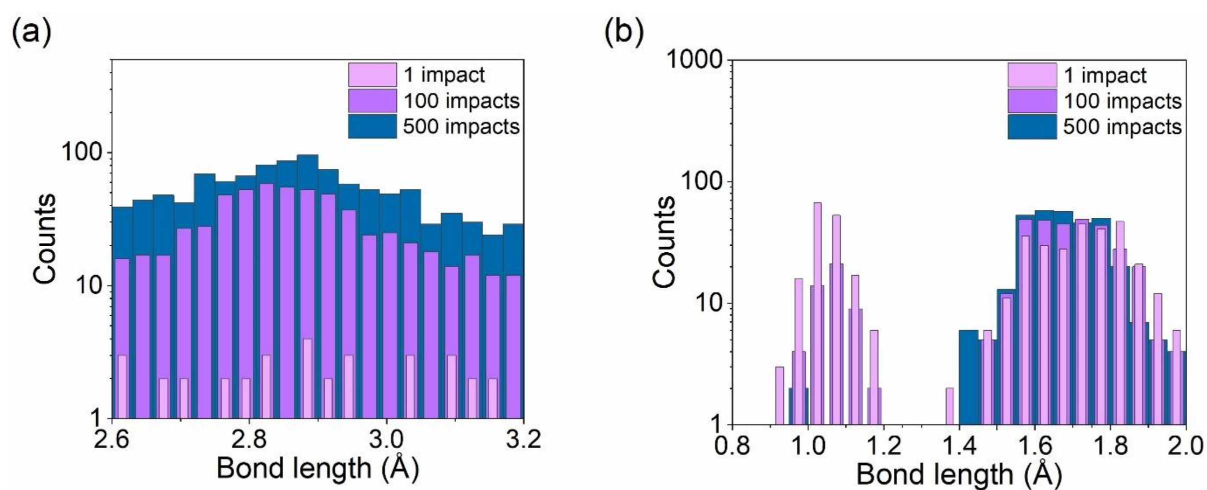

Figure 4: Evolution of bond lengths in the contaminated sample under bombardment. (a) 1st graph show bonds between 2.6 to 3.2 Å describing the amorphous layer formed

by Si – Si bonds, and (b) 2nd graph shows bonds between 1 and 2 Å describing O – X and H – X bonds.

Description of the amorphization

The two samples at several stages of the sputtering process are shown in **figure 5** to illustrate the evolution of the amorphization process. The penetration depth of argon atoms is limited to the first few lattices inside the silicon, for both the contaminated and clean sample. For the clean sample, the amorphization depth evolves linearly until the implanted argon atoms reach a saturation concentration due to the diffusion and desorption of excess atoms. In the contaminated sample, the observations are similar for argon and for the contaminants: hydrogen is implanted deeper than oxygen. Both also tends to be implanted deeper than argon, proportionally to their respective masses, but some occurences of deep argon implantation can happen. The amorphization can be decomposed into two phases:

- In an initial phase, most silicon atoms stay in their lattice position, even after receiving some energy from the incident argon ion, and only a small number of defects is formed. Water molecules are usually fragmented by an argon ion on the sample surface. The hydrogen and oxygen atoms being lighter than argon, they are pushed deeper into the sample, globally increasing the damage per collision. The argon ion is either backscattered or implanted. Previously implanted argon atoms can also diffuse to the sample surface when receiving enough energy. The different processes move gradually deeper into the sample with increasing fluence.
- The second phase is characterized by several impacts having happened in the close surroundings of a given region, and most atoms having been displaced from their initial equilibrium position. This phase describes an

amorphous layer. The depth of the amorphous layer varies as a function of the incidence angle and is maximum at around 70° with respect to the surface normal. In the amorphous region, contaminants and argon atoms reach a saturation concentration. Once argon saturation is reached, the thickness of the amorphous layer reaches a maximum, which is defined by the range of the argon atoms. At the same time, material is removed by sputtering from the surface.

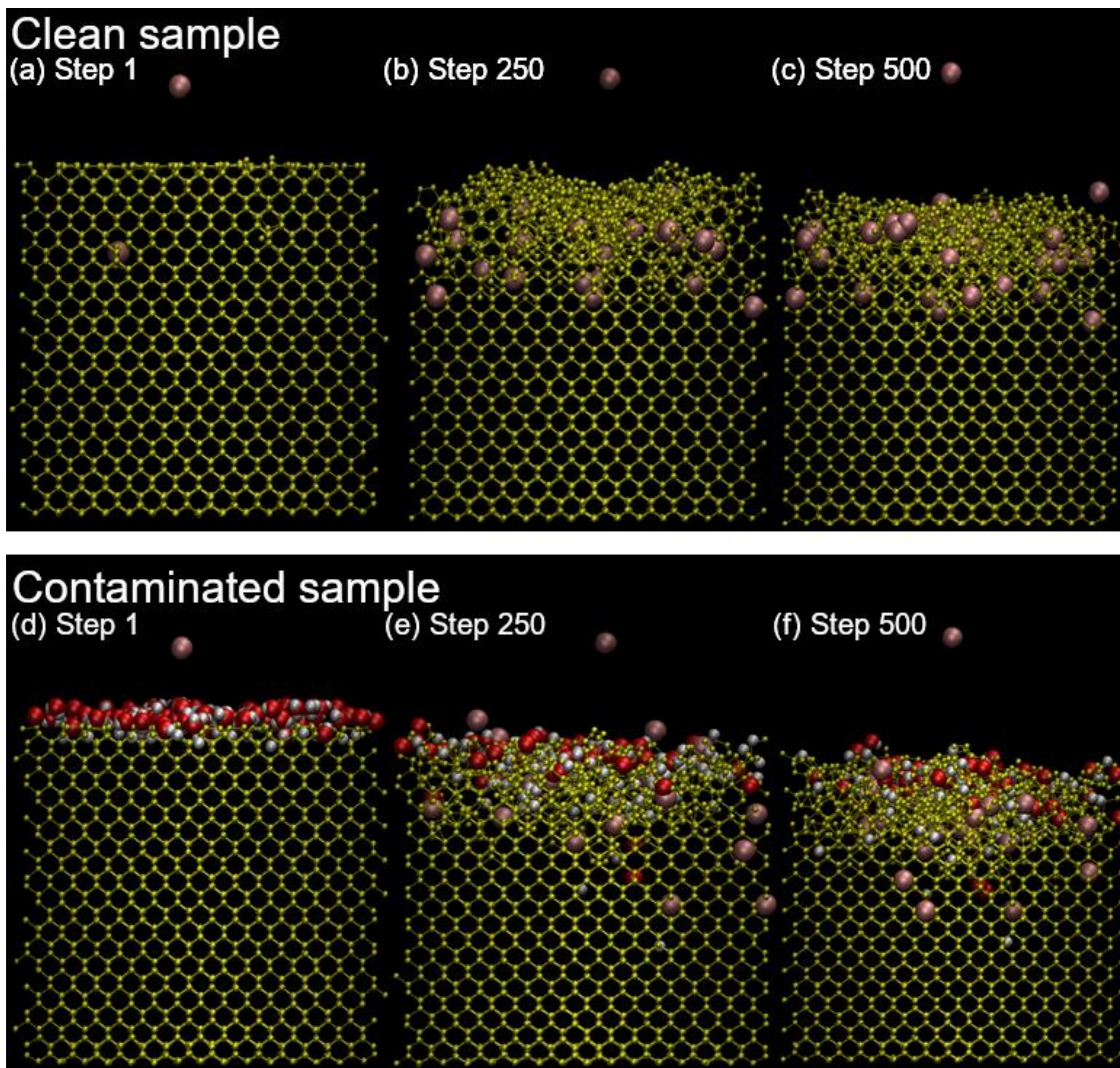

Figure 5: Evolution of the clean (a, b, c) and contaminated (d, e, f) sample under ion irradiation, before the 1st, 250th and 500th bombardment showing the evolution of the

sample's surface. The argon particle on top of the simulation is the ion being bombarded onto the sample.

Amorphization coefficient

To describe properly the amorphization process, we choose to monitor how the bond length distribution changes with the number of impacts. In particular, we calculated the coefficient described in equation (2):

$$\mu = \frac{1}{n_{Bonds}} \sum_{n_{Bonds}} \left[1 - \left| \frac{BondLength_{Theory} - BondLength_{Measured}}{BondLength_{Theory}} \right| \right] \quad (2)$$

To characterize the amorphization process as a function of depth, the simulation box was split into different slabs along the z direction, each slab having the height of one unit cell and the initial slab being situated on the bottom of the sample with an undisturbed surface. Then, the number of bonds and the bond lengths in each slice are calculated to obtain the μ coefficient associated to each slab. By comparing the different values of μ to the radial distribution functions of the different slabs, the data can be grouped in three different categories, i.e. the crystaline slabs, the semi-amorphous slab(s) and the amorphous slabs (cf. discussion on the rdf for more details):

- $0.94 < \mu < 1$ describes a region where no defects are present. Changes in μ are due to variations in bond length coming from thermal vibrations around the equilibrium bond length. This region is crystalline.
- $0.89 < \mu < 0.94$ describes regions that contain defects but are not completely amorphous, i.e. the crystalline structure is preserved at least in a small part of the slab. The collisions have only caused minor damages. For simplicity, we call this transitional phase a "partially-amorphous" or "semi-amorphous" region in the discussion.

- $\mu < 0.89$ designates slabs with almost no remaining crystalline structure. There is a large variance in bond lengths, generally describing a damaged / amorphous area with a lot of disorder.

A full breakdown of a sample bombarded by 0°, 45° and 75° argon ions, and the associated μ coefficients, can be found in the supplementary information, where each slab is detailed and compared with the associated radial distribution functions. As per design, the "semi-amorphous" layer is supposed to be 1 slab thick, as it is the transition between the amorphized region and the crystalline / intact part of the sample. In some cases, deeper penetration through chanelling of some atoms can cause a few slabs to be in the semi-amorphous regime. **Figure 6** shows the 3 regions in the sample, and **figure 7** represents the evolution of μ in the sample with respect to the depth of the slab, as well as with respect to the angle, describing how the ion's incidence angle influences the amorphization depth. The sample shows a continuous transition from crystalline to amorphous. A large difference is observed between pristine and contaminated samples at close to grazing incidence. For the pristine sample, the material is barely amorphized, whereas the presence of the contaminant leads to a full amorphization. In general, the incidence angle changes the depth at which the transition between amorphous and partially amorphized layer happens. At close to normal incidence, the demarcation is clear. At larger angles, the transition is shifted progressively closer towards the surface. Especially for angles above 83° there is almost no amorphous layer, the upper part of the sample being at most partially amorphized by the collisions. This can be explained by the fact that at such high angles the argon particles are mainly backscattered and interact very weakly with the sample. In the case of the contaminated sample, most of the damage is done via the fractioning of water molecules on the sample surface. The implantation of argon ions is minimal.

Compared to other existing methods, our solution uses only the nearest neighbours of a given atom, which allows for a faster computation when using a large number of atoms. The results show that with increasing disorder, the amorphization can be described by the change in bond lengths, and bond angles. Therefore, the variation and distribution of angles in the amorphous region evolve to a point where all the angular distribution information becomes irrelevant. A methodology based on the averaged bond order parameters would hence become very time consuming for a larger scale sample (compared to the methodology by Lechner et. al.[36]). On the other hand, a method using a local-order metric as described in the paper by *Martelli et. al.*[37] can be used for a whole sample, but in the current study the information on the transition of the crystal structure between different regions cannot be obtained. For these reasons, we developed our methodology, i.e. a bond centric analysis based on the definition of regions. Furthermore, by using a local-order metric, the high degree of overlapping would make it difficult to observe the precise region where the transition between each region previously defined would happen.

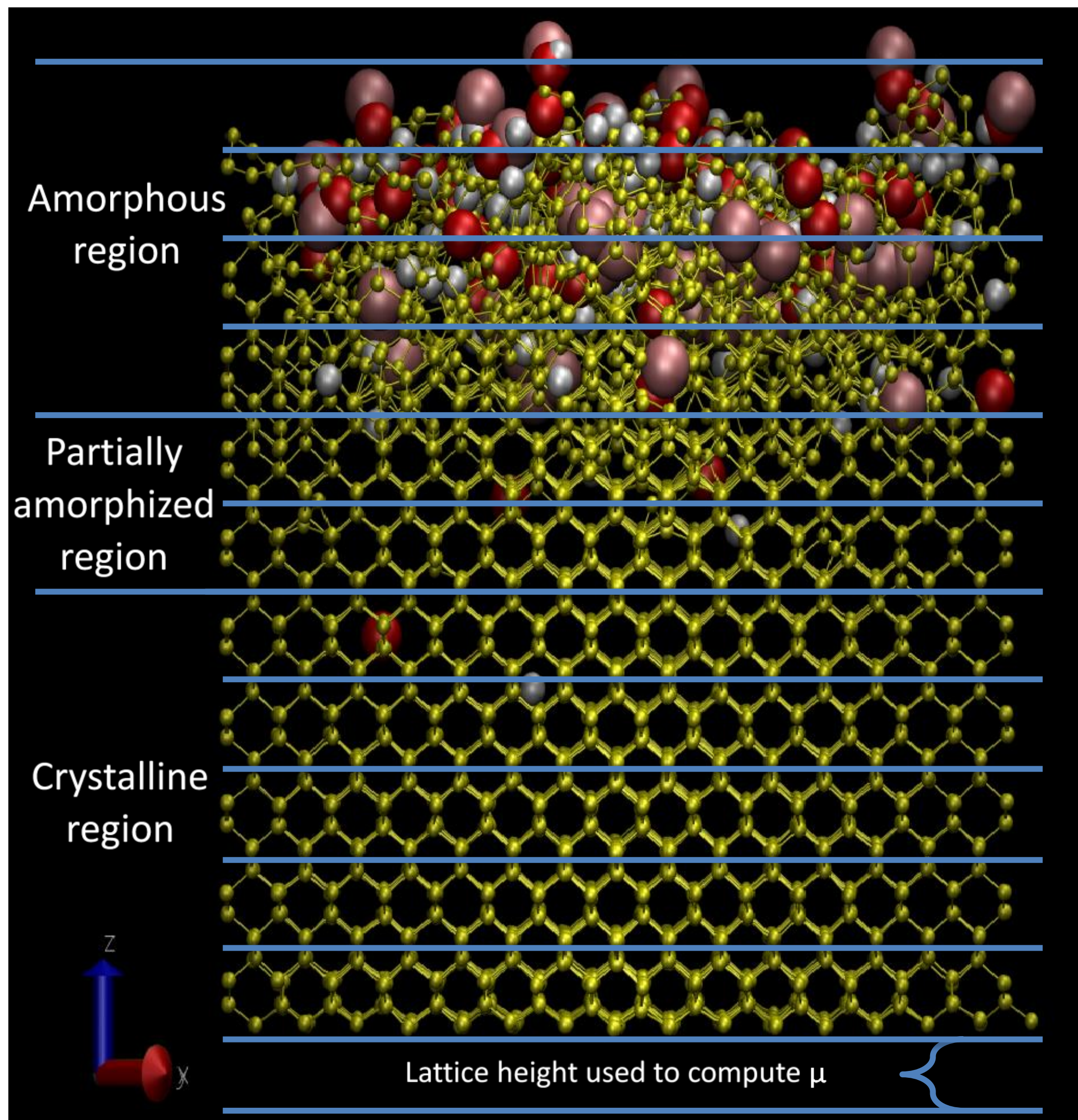

Figure 6: Representation of each region in the sample, the amorphous region being the one with the highest disorder, the crystalline region being the one with the lowest disorder, and the partially amorphized region representing the transition between the two regions.

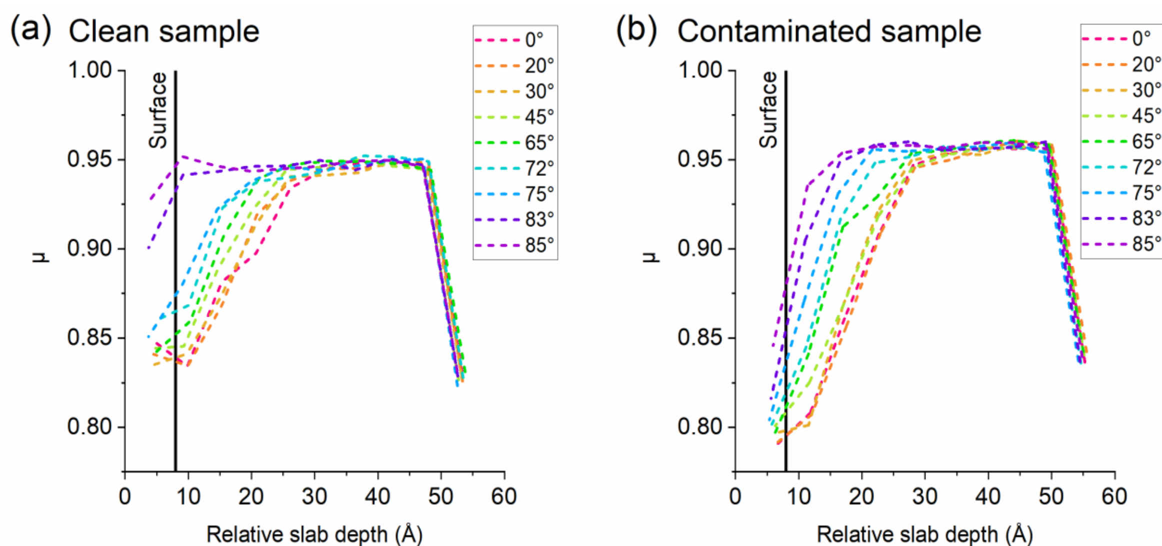

Figure 7: Evolution of the μ coefficient with respect to the angle, for (a) the pristine sample and (b) the contaminated sample. The last data point at 55 Å has a low value in the 0.825 - 0.850 region due to the non-periodicity along the Z axis in the simulation, causing the formation of dimers on the bottom of the sample.

Radial distribution function

The radial distribution function (RDF) has been calculated for the different slabs to support the findings of the previous section. The algorithm used to calculate RDF in finite non-periodic samples can be found in the article written by *Kopera et. al.*[54] With the previously defined slabs, it is possible to calculate the RDF for each region, showing clear differences in the local structural coherency. **Figure 8** shows the RDF for each slab in the pristine and contaminated samples. A first observation is the difference between each slab's RDF: the amorphous layer has almost no coherency whereas the crystalline slabs have a strong local order and patterns repeating past the 2nd nearest neighbors, i.e., for the crystalline structures the peaks above 5 Å are still well defined while the different peaks are not separated for the amorphous structure.

The semi-amorphous region shows some coherency after the 2nd neighbor peak but with some characteristics of the amorphous RDF.

We can also observe the difference between clean and contaminated sample in **figure 9**: For the clean sample, a smaller peak appears between the 2nd and 3rd peak, in the 2.6 to 3.2 Å region. These bonds are due to defect production in silicon after argon irradiation. For the contaminated sample, the same peak can be observed, and another peak appears in the 1.5 Å region which is created by the Si – H and Si – O bonds due to fragmentation of the water molecules. From these observations we can determine the influence of the incidence angle on the amorphization process by comparing the RDF slab's (**figure 10)**. When comparing the RDF at more grazing angles for the clean and contaminated samples, there is less damage directly done by argon ions, but more damage comes from the hydrogen and oxygen atoms mixed into the sample. Due to grazing incidence, most argon ions are backscattered but the deposited energy is high enough to split the water molecules and push hydrogen and oxygen atoms deeper into the sample. As hydrogen is very light it can travel further into the sample, channel through the lattices and go preferentially into interstitial sites. The same reasoning applies to oxygen except that it implants at a lower depth due to the higher mass which makes channeling less likely. At higher angles, the amorphous slab's RDF is almost identical to the semi-amorphous' region, meaning that the disorder created by the collisions is marginal and the variations of the μ coefficient of the slab are minimal. In the next section, the implantation depths of argon, hydrogen and oxygen will be discussed to understand their impact on the amorphization process.

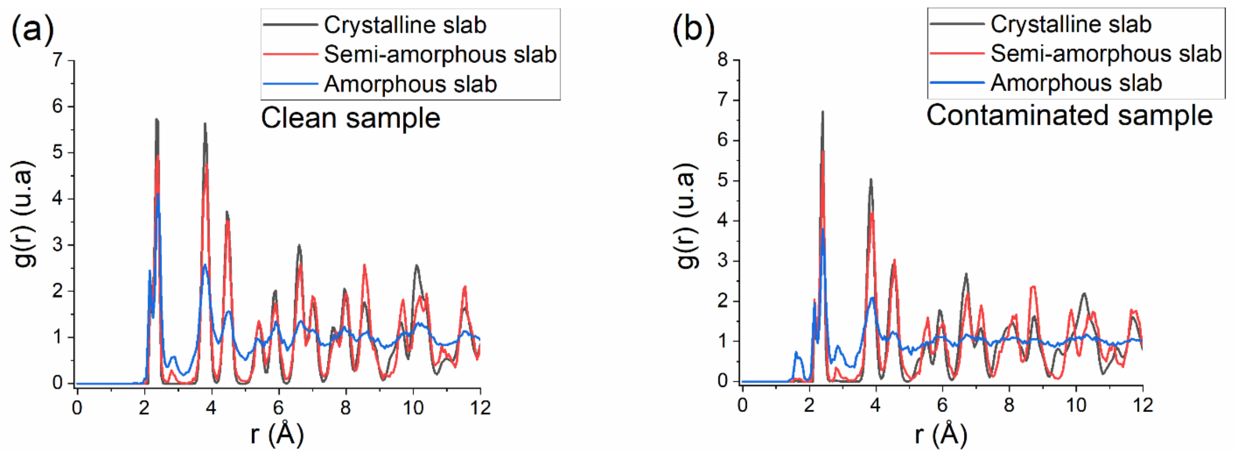

Figure 8: Radial distribution function for (a) clean and (b) contaminated sample for all previously determined regions. Hard limit fixed 12 Å representing 2.5 lattices (or more than 10 neighbors).

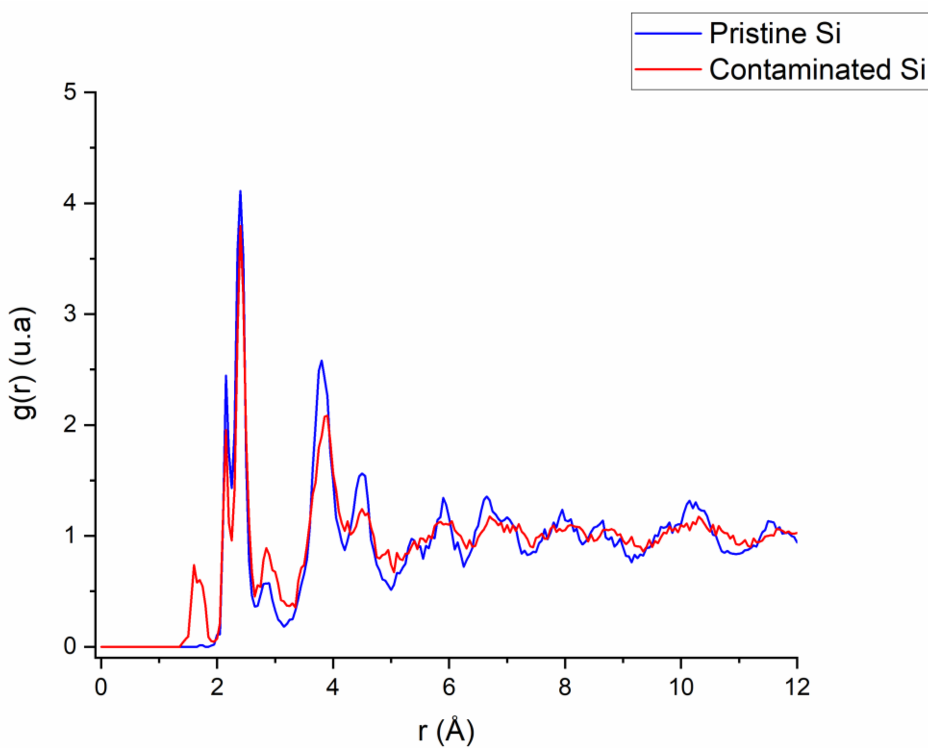

Figure 9: Comparison for the radial distribution function for both samples in the amorphous layer. The same cut-off of 12Å is applied.

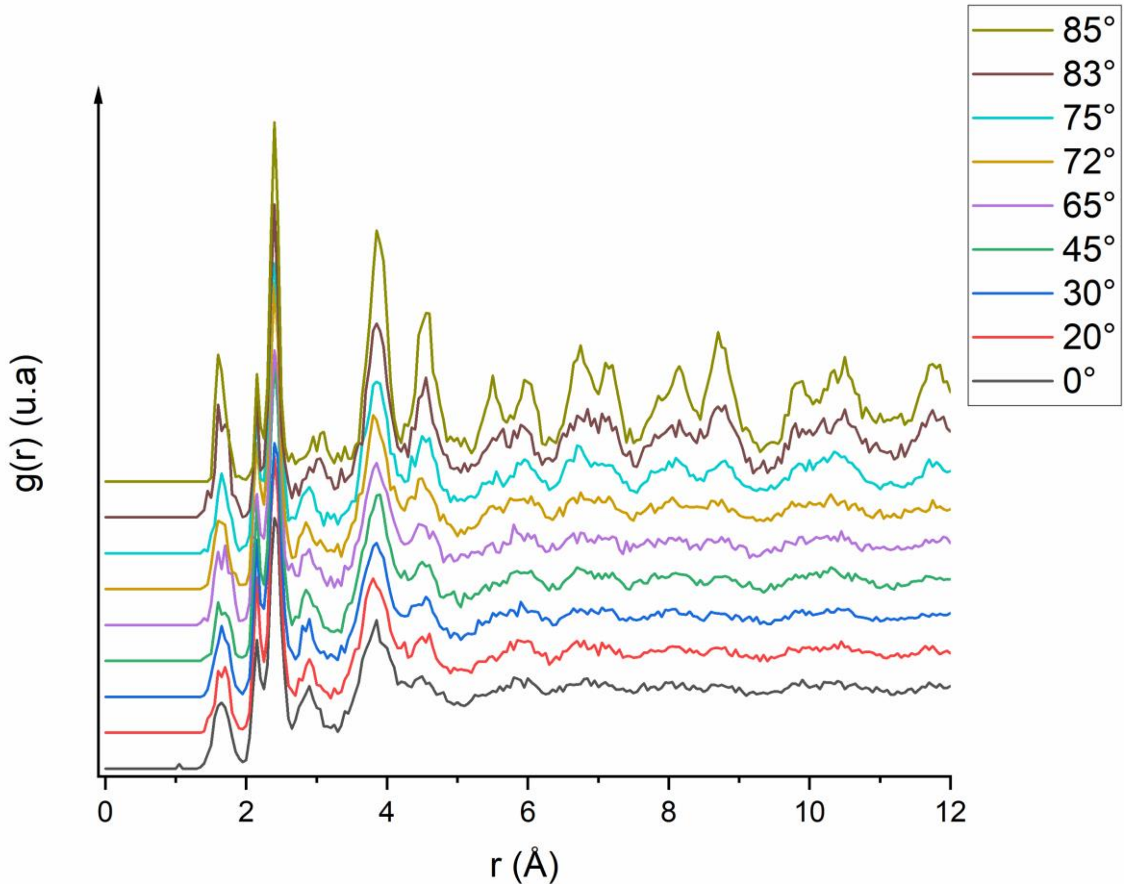

Figure 10: Comparison of the radial distribution function in the amorphous slab of the contaminated sample with respect to the angle of impact. The angles selected for this study are listed above and aim to cover angles between 0° and 85°.

Ion implantation

The implantation depth of each chemical element (e.g. hydrogen, oxygen and argon) and the number of implanted atoms vary greatly with respect to the incidence angle. At grazing incidence, argon is not implanted but backscattered. For the contaminated sample, the argon can fragment water molecules even at grazing incidence. Hydrogen and oxygen atoms displaced at the same surface by an incident argon ion are either sputtered or implanted into the sample, causing damage significantly deeper than the

damage observed for the pristine sample, as shown in the **figure 11**. At low fluences, most atoms will not be involved in collision cascades, but with increasing fluence, i.e. with the number of impacts going up to 500, almost all atoms of the surface will be displaced from their initial position and all water molecules will be eventually destroyed. After getting some energy in an atomic collision, the direction of hydrogen or oxygen atoms allows in some situations for channeling, leading to a deeper penetration into the bulk without causing damage.

The biggest difference between pristine and contaminated sample is also observed in these high angles (80° and above), where in the pristine sample most of the interactions are located on the surface, but in the contaminated sample hydrogen and oxygen are causing damage deeper in the sample. Since these angles are commonly used for the final polishing in the TEM lamella preparation, it is interesting to understand the impact of water in this specific case.

To quantify the impact of contaminants on the irradiation process, we looked at the distributions of argon particles and compared it to the distribution of contaminants for each incidence angle. The result of these comparisons can be found in the **figure 12**. For angles above 80°, we can see that argon is not implanted into the sample, all of them being backscattered. Like the contaminant distribution, we can see some implantation deeper than the depth of the amorphous slab.

Furthermore, the mean implantation depth of hydrogen is twice as deep than the one of oxygen. This behavior can be explained by two factors:

- Hydrogen atoms are involved twice as often than oxygen in displacements, due to the number of atoms of each species in the water molecule. In the early stage of the sputtering process, this is true since the water molecules are intact, and therefore the collision will either sputtering or fragmenting the molecules. During the latter events, hydrogen and oxygen might be pushed

into the sample. At higher fluences, where most of the hydrogen atoms are dissociated from oxygen atoms, the probability of hydrogen being involved in a collision cascade is twice as high than for oxygen, because the ratio between the two species stays approximately constant throughout the process.

- Hydrogen being lighter than oxygen, the particle can channel easily through the silicon lattice and penetrate deeper into the sample. This phenomenon can happen if the hydrogen is impacted at the correct angle, either by initial collisions with argon ions or by recoil atoms during the collision cascade. This will allow it to travel in a straight path through the silicon lattice, reaching and causing damage in deeper regions.

Overall, the contaminant will be displaced into the amorphous region of the sample, causing this region to be thicker than for the pristine sample. This effect can impact the preparation of samples such as ultra-thin lamellas for TEM.

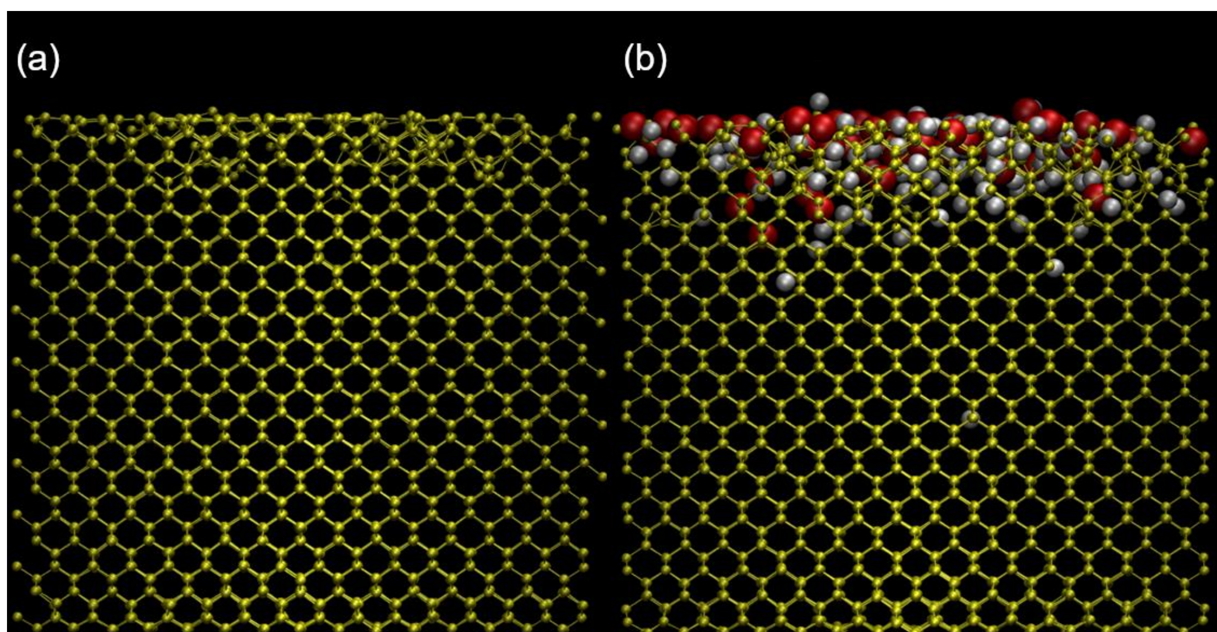

Figure 11: Comparison between samples after an irradiation with incident beam at 100 eV and 85° for (a) the pristine sample and (b) the contaminated sample, where the

silicon particles are in the compact representation (yellow) and the oxygen (red) and hydrogen (white) are represented with their Van der Waals interaction sphere.

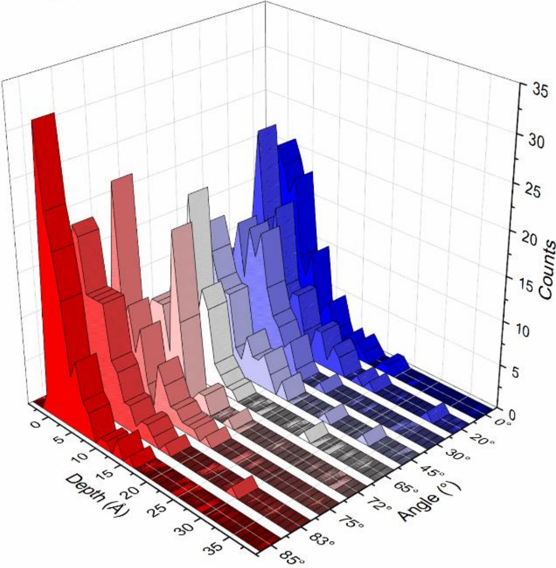

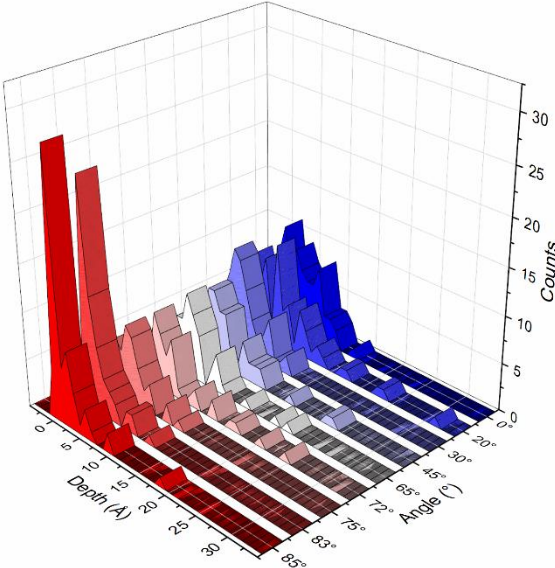

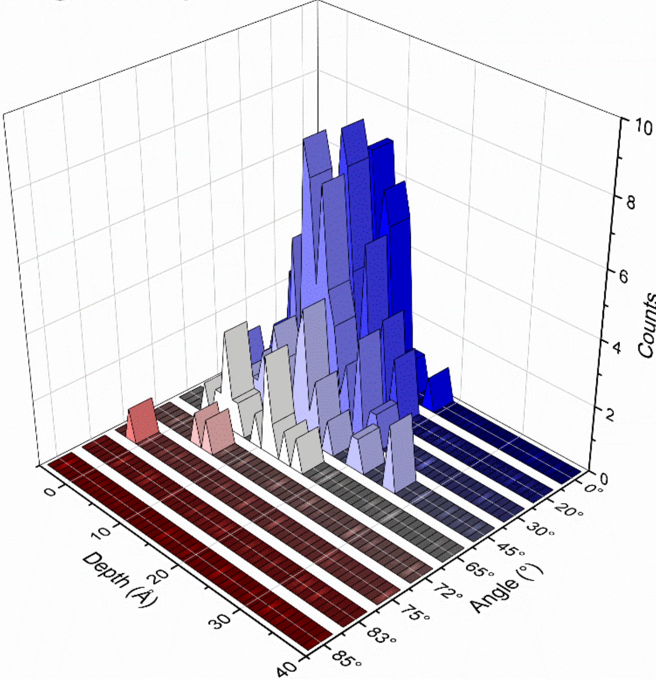

Figure 12: Distribution of implanted contaminants, (a) oxygen, (b) hydrogen and (c) argon, with respect to the selected angles.

Sputtering yields

Sputtering yields are important for experiments as they define how quickly a sample is eroded. Here, we compare the sputtering yields of pristine and contaminated samples averaged over the 500 impacts (**figure 13**). No significant difference can be observed between the silicon sputtering yields coming from the pristine and contaminated sample. As expected, both sputtering yields increase with increasing incidence angle to reach a maximum around 65 degrees. For the partial sputtering yields of hydrogen and oxygen, the curves are flatter and reach their maximum values for incidence angles in the 70 degrees, i.e. for more grazing incidence than silicon. The total sputtering yield of the contaminated sample, i.e. the sum of silicon, oxygen and hydrogen partial sputtering yields, is much higher than the sputtering yield of the pristine sample, showing that the water molecules are sputtered quite easily.

A second parameter of interest related to sputtering is the sputtered fraction of hydrogen and oxygen atoms (**figure 14**). At normal incidence about 25% of the hydrogen and oxygen atoms are sputtered, meaning that by far the largest fraction is implanted and only few stay on the sample surface. This can be explained by the velocity vector of argon ions being oriented straight into the sample, and this orientation being maintained for the energy transfer to the target atoms. Interestingly, the partial sputtering yields of the hydrogen and oxygen atoms are highest at incidence angles between 70 and 80 degrees, i.e. above angles where the silicon sputtering yields are highest, leading to the sputtering of about 75% of the adsorbed molecules. At these angles, most argon ions are backscattered but the energy transfer is still high enough to fragment the water molecules and induce the sputtering of hydrogen and oxygen atoms. Hence, if the implantation of surface contaminations should be minimized in experiments, the incidence angle should be chosen in this range.

In the current simulations, the water layer was added before argon irradiation was started. When renewing the water layer during the irradiation process, as it happens during experiments, the partial sputtering yield of silicon might be lowered by the presence of the surface contamination, at least if the contamination level is above a

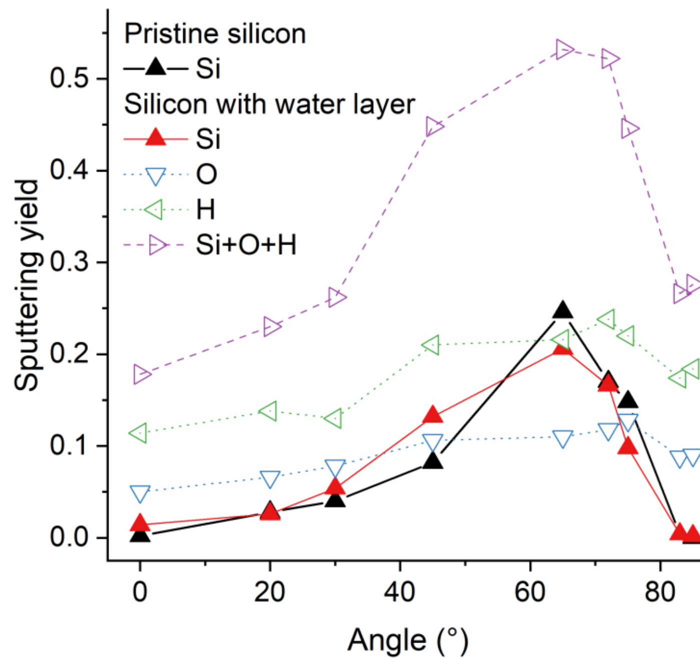

critical threshold.

Figure 13: Sputtering yields of the pristine and contaminated sample with respect to the angle. In the contaminated sample sputter yields, we make the distinction between all sputtered particles (sum of partial sputtering yields of oxygen, hydrogen and silicon – hollow purple triangles) and the silicon (full red and black triangles) / contaminants (hollow blue and green triangles) only counts.

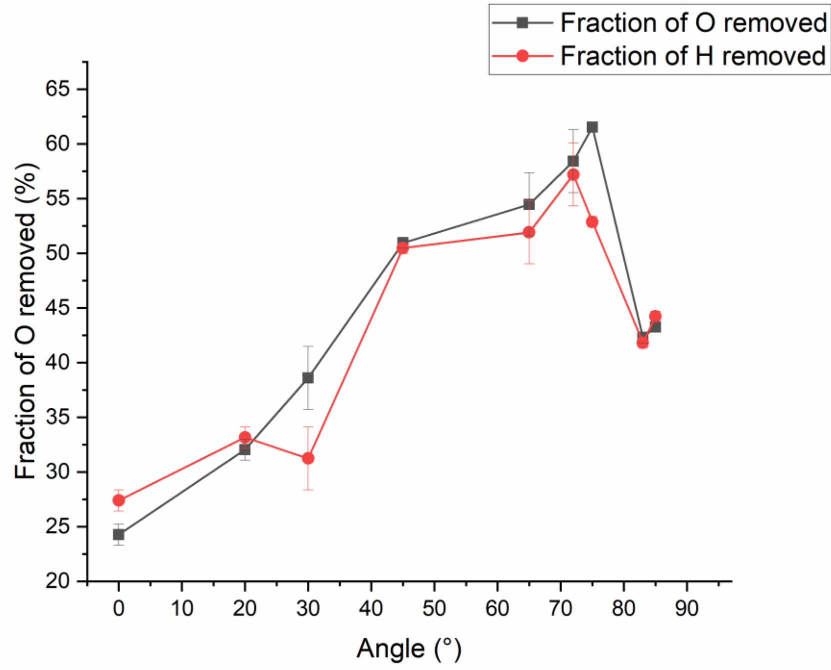

Figure 14: Fraction of the contaminants sputtered after 500 impacts with respect to the angle. The values are represented in percentage of the total particles removed, by counting the contaminant particles in the initial sample and deducting the counts in the final steps, for each angle.

Conclusion

In this work, we analyzed the influence of the incidence angle on 100 eV sputter processes using MD simulations for the irradiation with argon ions of silicon samples with a clean surface and covered with a monolayer of water molecules. Contaminants adsorbed on the sample surface amplify the damage done by the argon ions. A methodology based on the modification of bond lengths has been developed to characterize the irradiation-induced damage. Three regions have been identified in the sample, (i) a totally amorphous layer closer to the surface, (ii) a transitive, partially amorphized layer presenting defects and, (iii) the crystalline region underneath that remains unaffected by the ion irradiation. At closer to grazing incidence (e.g. above 75°), argon implantation becomes sparse but the fragmentation and sputtering of water molecules is maximum. Hence, sputtering yields and molecular fragmentation show that specific angles can be selected to reduce the mixing of contaminants into the sample in ultra-low energy sputtering. Compared to the pristine sample, the mixing of hydrogen and oxygen atoms into the sample increases the overall degree of amorphization.

In this study, the water layer on the silicon surface was prepared before ion irradiation and not renewed during the milling process. However, in experiments contaminations adsorb continuously on the sample surface, leading to a renewal of the contamination layer. Furthermore, at higher impact energy the implantation depth of the ions is increased, leading most likely to a different amorphization process. Both aspects will be explored in future studies.

Supporting Information

Supporting information summary:

DFT data fitting plots

Graph 1. Plot of the Ar – Si details with fitting parameters D_0, α and r_0 used in the LAMMPS script to output the potential. The full potential is displayed

Graph 2. Plot of the Ar – Si details with fitting parameters D_0, α and r_0 used in the LAMMPS script to output the potential. A focused part is displayed, putting accent on the potential well describing the inter-atomic forces (switch from repulsive to attractive part of the potential).

Graph 3. Plot of the Ar – O details with fitting parameters D_0, α and r_0 used in the LAMMPS script to output the potential. The full potential is displayed

Graph 4. Plot of the Ar – O details with fitting parameters D_0, α and r_0 used in the LAMMPS script to output the potential. A focused part is displayed, putting accent on the potential well describing the inter-atomic forces (switch from repulsive to attractive part of the potential).

Graph 5. Plot of the Ar – H details with fitting parameters D_0, α and r_0 used in the LAMMPS script to output the potential. The full potential is displayed

Graph 6. Plot of the Ar – H details with fitting parameters D_0, α and r_0 used in the LAMMPS script to output the potential. A focused part is displayed, putting accent on the potential well describing the inter-atomic forces (switch from repulsive to attractive part of the potential).

Graph 7. Plot of the Ar – Ar details with fitting parameters D_0, α and r_0 used in the LAMMPS script to output the potential. The full potential is displayed

Graph 8. Plot of the Ar – Ar details with fitting parameters D_0, α and r_0 used in the LAMMPS script to output the potential. A focused part is displayed, putting accent on

the potential well describing the inter-atomic forces (switch from repulsive to attractive part of the potential).

G(r) per slab and grouping details

Graph 9..Plot of the detailed radial distribution functions for each slabs, with a color grading depending of the region for 100 ev, 0° bombardements, after 500 simulations

Graph 10..Plot of the detailed radial distribution functions for each slabs, with a color grading depending of the region for 100 ev, 45° bombardements, after 500 simulations

Graph 11..Plot of the detailed radial distribution functions for each slabs, with a color grading depending of the region for 100 ev, 75° bombardements, after 500 simulations

ReaxFF Potential

Table 1. Force field parameters, from "Oxidation of Silicon Carbide by O2 and H2O: A ReaxFF Reactive Molecular Dynamics Study, Part I" by David A. Newsome. et. al. - *J. Phys. Chem. C* 2012, 116, 30, 16111–16121.

Supporting Information File:

Ar_Si_Angles_Publication_Final_Version_Supporting_Information_03092022.docx

File Format: Word document (.docx)

Acknowledgements

The Luxembourg National Research Fund (FNR) is thanked for the financial support provided through the grant C17/MS/11682850/ULOWBEAM. Dr. Chad Rue, Dr. Richard J. Young from Thermo Fisher Scientific and Dr. Tom Wirtz from Luxembourg Institute of Science and Technology are acknowledged and thanked for all the fruitful discussions and their comments during the writing process.

Funding

This project was supported by the National Research Fund (FNR), Luxembourg (C17/MS/11682850/ULOWBEAM).

References

(1) Wirtz, T.; De Castro, O.; Audinot, J.-N.; Philipp, P. *Annu. Rev. Anal. Chem.* **2019**, *12* (1), 523–543. doi:10.1146/annurev-anchem-061318-115457

(2) Pillatsch, L.; Östlund, F.; Michler, J. *Prog. Cryst. Growth Charact. Mater.* **2019**, *65*, 1–19. doi:10.1016/j.pcrysgrow.2018.10.001

(3) Audinot, J.-N.; Philipp, P.; Castro, O. De; Biesemeier, A.; Hoang, Q. H.; Wirtz, T. *Reports Prog. Phys.* **2021**, *84* (10), 105901. doi:10.1088/1361-6633/AC1E32

(4) Wirth, R. *Chem. Geol.* **2009**, *261* (3–4), 217–229. doi:10.1016/j.chemgeo.2008.05.019

(5) Thermoscientific. **2018**, 1–4

(6) McPhail, D. S. *J. Mater. Sci.* **2006**, *41* (3), 873–903. doi:10.1007/s10853-006-6568-x

(7) Tseng, A. A. *Small* **2005**, *1* (10), 924–939. doi:10.1002/smll.200500113

(8) Kawasegi, N.; Yamaguchi, M.; Kozu, T.; Morita, N.; Nishimura, K. *Precis. Eng.* **2017**, *50*, 337–343. doi:10.1016/J.PRECISIONENG.2017.06.007

(9) Hasan, R. M. M.; Luo, X. *ICAC 2017 - 2017 23rd IEEE Int. Conf. Autom. Comput. Addressing Glob. Challenges through Autom. Comput.* **2017**, 1–6. doi:10.23919/ICONAC.2017.8081979

(10) Sloyan, K.; Melkonyan, H.; Apostoleris, H.; Dahlem, M. S.; Chiesa, M.; Ghaferi, A. Al. *Nanotechnology* **2021**, *32* (47), 472004. doi:10.1088/1361-6528/AC1D75

(11) Llobet, J.; Krali, E.; Wang, C.; Arbiol, J.; Jones, M. E.; Pérez-Murano, F.; Durrani,

Z. A. K. *Appl. Phys. Lett.* **2015**, *107* (22), 223501. doi:10.1063/1.4936757

(12) Córdoba, R.; Mailly, D.; Rezaev, R. O.; Smirnova, E. I.; Schmidt, O. G.; Fomin, V. M.; Zeitler, U.; Guillamón, I.; Suderow, H.; Teresa, J. M. De. *Nano Lett.* **2019**, *19* (12), 8597–8604. doi:10.1021/ACS.NANOLETT.9B03153

(13) De Teresa, J. M.; Orús, P.; Córdoba, R.; Philipp, P. *Micromachines* **2019**, *10* (12). doi:10.3390/mi10120799

(14) Philipp, P.; Ngo, Q. K.; Shtein, M.; Kieffer, J.; Wirtz, T. *Anal. Chem.* **2013**, *85* (1), 381–388. doi:10.1021/ac302939m

(15) Prokhodtseva, A.; Mulders, J.; Vystavel, T. *Microsc. Microanal.* **2017**, *23* (S1), 298–299. doi:10.1017/s1431927617002173

(16) Lécz, Z.; Budai, J.; Andreev, A.; Ter-Avetisyan, S. *Phys. Plasmas* **2020**, *27* (1). doi:10.1063/1.5123542

(17) Azuma, Y.; Kurokawa, A. *X-Ray Spectrom.* **2019**, *48* (5), 345–350. doi:10.1002/xrs.3006

(18) Barry, P. R.; Philipp, P.; Wirtz, T.; Kieffer, J. *J. Mass Spectrom.* **2014**, *49* (3), 185–194. doi:10.1002/jms.3317

(19) MacH, J.; Šamoil, T.; Voborn, S.; Kolíbal, M.; Zlámal, J.; Spousta, J.; Dittrichov, L.; Šikola, T. *Rev. Sci. Instrum.* **2011**, *82* (8). doi:10.1063/1.3622749

(20) Rzeznik, L.; Fleming, Y.; Wirtz, T.; Philipp, P. *Beilstein J. Nanotechnol.* **2016**, *7*, 1113–1128. doi:10.3762/bjnano.7.104

(21) Yoshigoe, A.; Teraoka, Y. *Surf. Sci.* **2003**, *532–535*, 690–697. doi:10.1016/S0039-6028(03)00412-6

(22) Pal, G.; Yadav, R. C.; Akhter, J.; Das, T.; Sarkar, A.; Mallik, C.; Bhandari, R. K. *J. Phys. Conf. Ser.* **2012**, *390* (1), 1–6. doi:10.1088/1742-6596/390/1/012045

(23) Forrest, E.; Schulze, R.; Liu, C.; Dombrowski, D. *Int. J. Heat Mass Transf.* **2015**, *91*, 311–317. doi:10.1016/j.ijheatmasstransfer.2015.07.112

(24) Zhang, W.; Van Duin, A. C. T. *J. Phys. Chem. B* **2017**, *121* (24), 6021–6032. doi:10.1021/acs.jpcb.7b02548

(25) Yeon, J.; Van Duin, A. C. T.; Kim, S. H. *Langmuir* **2016**, *32* (4), 1018–1026. doi:10.1021/acs.langmuir.5b04062

(26) Fogarty, J. C.; Aktulga, H. M.; Grama, A. Y.; Van Duin, A. C. T.; Pandit, S. A. *J. Chem. Phys.* **2010**, *132* (17). doi:10.1063/1.3407433

(27) Smith, R.; Don E. Harrison, J.; Garrison, B. J. KeV Particle Bombardment of Semiconductors: A Molecular-Dynamics Simulation. Physical Review B 1989, p 9. doi:10.1103/physrevb.40.93

(28) Gras-Marti, A.; Kirchner, R.; Smith, R.; Webb, R. P.; Beardmore, K. *Nucl. Instruments Methods Phys. Res. Sect. B Beam Interact. with Mater. Atoms* **2009**, *102* (1–4), 211–217. doi:10.1016/0168-583x(95)80143-a

(29) Stillinger, F. H.; Weber, T. A. Fluorination of the Dimerized Si(100) Surface Studied by Molecular-Dynamics Simulation. *Physical Review Letters*. 1989, pp 2144–2147. doi:10.1103/PhysRevLett.62.2144

(30) Senftle, T. P.; Hong, S.; Islam, M. M.; Kylasa, S. B.; Zheng, Y.; Shin, Y. K.; Junkermeier, C.; Engel-Herbert, R.; Janik, M. J.; Aktulga, H. M.; Verstraelen, T.; Grama, A.; Van Duin, A. C. T. *npj Comput. Mater.* **2016**, *2* (November 2015). doi:10.1038/npjcompumats.2015.11

(31) Abolfath, R. M.; Van Duin, A. C. T.; Brabec, T. *J. Phys. Chem. A* **2011**, *115* (40), 11045–11049. doi:10.1021/jp204894m

(32) Kowalik, M.; Hossain, M. J.; Lele, A.; Zhu, W.; Banerjee, R.; Granzier-Nakajima, T.; Terrones, M.; Hudson, E. W.; van Duin, A. C. T. *Catalysts* **2021**, *11* (2), 1–12. doi:10.3390/catal11020208

(33) Chenoweth, K.; Van Duin, A. C. T.; Goddard, W. A. *J. Phys. Chem. A* **2008**, *112* (5), 1040–1053. doi:10.1021/jp709896w

(34) Newsome, D. A.; Sengupta, D.; Foroutan, H.; Russo, M. F.; Van Duin, A. C. T. *J. Phys. Chem. C* **2012**, *116* (30), 16111–16121. doi:10.1021/jp306391p

(35) Soria, F. A.; Zhang, W.; Paredes-Olivera, P. A.; Van Duin, A. C. T.; Patrito, E. M. *J. Phys. Chem. C* **2018**, *122* (41), 23515–23527. doi:10.1021/acs.jpcc.8b07075

(36) Lechner, W.; Dellago, C. *J. Chem. Phys.* **2008**, *129* (11). doi:10.1063/1.2977970

(37) Martelli, F.; Ko, H. Y.; Oğuz, E. C.; Car, R. *Phys. Rev. B* **2018**, *97* (6), 4–9. doi:10.1103/PhysRevB.97.064105

(38) Goddard, W. A.; Duin, A. C. T. Van; Strachan, A.; Stewman, S.; Zhang, Q.; Xu, X. *J. Phys. Chem. A* **2003**, *107* (19), 3803–3811

(39) Costa Filho, R. N.; Alencar, G.; Skagerstam, B. S.; Andrade, J. S. *EPL* **2013**, *101* (1). doi:10.1209/0295-5075/101/10009

(40) pair _ style hybrid command — LAMMPS documentation. https://docs.lammps.org/pair_hybrid.html.

(41) Rappe, A. K.; Goddard III, W. A. *J. Phys. Chem.* **1991**, *95* (8340), 3358–3363

(42) Aiichiro, N. *Comput. Phys. Commun.* **1997**, *104* (1–3), 59–69

(43) Aktulga, H. M.; Fogarty, J. C.; Pandit, S. A.; Grama, A. Y. *Parallel Comput.* **2012**, *38* (4–5), 245–259. doi:10.1016/j.parco.2011.08.005

(44) Plimpton, S. Fast Parallel Algorithms for Short-Range Molecular Dynamics. *Journal of Computational Physics*. 1995, pp 1–19. doi:10.1006/jcph.1995.1039

(45) Kamiyama, E.; Sueoka, K. *J. Electrochem. Soc.* **2010**, *157* (3), H323. doi:10.1149/1.3281184

(46) Grønbech-Jensen, N.; Farago, O. *Mol. Phys.* **2013**, *111* (8), 983–991. doi:10.1080/00268976.2012.760055

(47) Chen, J.; Zhang, G.; Li, B. *J. Phys. Soc. Japan* **2010**, *79* (7), 1–18. doi:10.1143/JPSJ.79.074604

(48) Simonton, R. B.; Kamenitsa, D. E.; Ray, A. M.; Park, C.; Klein, K. M.; Tasch, A. F. *Nucl. Inst. Methods Phys. Res. B* **1991**, *55* (1–4), 39–44. doi:10.1016/0168-583X(91)96132-5

(49) Stegmann, H.; Ritz, Y.; Utess, D.; Hübner, R.; Zschech, E. *AIP Conf. Proc.* **2009**, *1173* (October 2009), 275–279. doi:10.1063/1.3251233

(50) Demaison, J.; Herman, M.; Lievin, J. *Int. Rev. Phys. Chem.* **2007**, *26* (3), 391–420. doi:10.1080/01442350701371919

(51) Van de Walle, C. *Phys. Rev. B - Condens. Matter Mater. Phys.* **1999**, *59* (20), 12884–12889. doi:10.1103/PhysRevB.59.12884

(52) Baur, W. H. *Acta Crystallogr. Sect. B Struct. Crystallogr. Cryst. Chem.* **1977**, *33* (8), 2615–2619. doi:10.1107/s0567740877009029

(53) Niu, C. Y.; Wang, J. T. *J. Chem. Phys.* **2013**, *139* (19), 1–6. doi:10.1063/1.4832340

(54) Kopera, B. A. F.; Retsch, M. *Anal. Chem.* **2018**, *90* (23), 13909–13914. doi:10.1021/acs.analchem.8b03157

Table of content entry